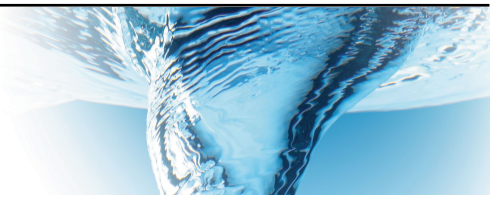
J. Fluid Mech. (2025), *vol.* 1019, R4, doi:10.1017/jfm.2025.10630



Three-dimensional low-frequency dynamics of a turbulent separation bubble

Ben Steinfurth[1], **Mogeng Li**[2,3], **Fulvio Scarano**[2] **and Julien Weiss**[1]

[1]Chair of Aerodynamics, Technische Universität Berlin, Berlin 10587, Germany

[2]Aerodynamics Section, Delft University of Technology, HS Delft 2629, The Netherlands

[3]School of Aerospace, Mechanical and Mechatronic Engineering, University of Sydney, Darlington 2008, NSW, Australia

Corresponding author: Ben Steinfurth, ben.steinfurth@tu-berlin.de

(Received 10 June 2025; revised 6 August 2025; accepted 16 August 2025)

Turbulent separating and reattaching flows are known to exhibit low-frequency fluctuations manifested in a large-scale contraction and expansion of the reverse-flow region. Previous experimental investigations have been restricted to planar measurements, while the computational cost to resolve the low-frequency spectrum with high-fidelity simulations currently appears to be unaffordable. In this article, we make use of volumetric measurements to reveal the low-frequency dynamics of a turbulent separation bubble (TSB) formed in the fully turbulent flow past a smooth backward-facing ramp. The volumetric velocity field measurements cover the entire separated flow region over a domain with a spanwise extent of $S = 0.6\,\mathrm{m}$. Spectral proper orthogonal decomposition (SPOD) of the velocity fluctuations reveals low-rank low-frequency behaviour at Strouhal numbers $St < 0.05$, which was also observed in previous planar measurements. However, in contrast with the interpretation of a two-dimensional contraction/expansion motion, the low-frequency dynamics is shown to be inherently three-dimensional, and governed by large elongated structures with a spanwise wavelength of approximately $S/2$. A low-order model constructed with the leading SPOD mode confirms substantial changes of the TSB extent in the centre plane, linking it to the modal pattern that is strongly non-uniform in the spanwise direction. The findings presented in this study promote a more complete understanding of the low-frequency dynamics in turbulent separated flows, thereby enabling novel modelling and control approaches.

Key words: boundary-layer separation

1. Introduction

Turbulent boundary-layer separation can have significant implications for engineering and environmental flows. In aerodynamics applications, for example, separation is typically

© The Author(s), 2025. Published by Cambridge University Press.

https://doi.org/10.1017/jfm.2025.10630 Published online by Cambridge University Press

associated with a drag increase and a loss of lift. Such detriments are exacerbated by the unsteady nature of turbulent flow separation, potentially yielding noise emission and severely fluctuating thermal and mechanical loads. Understanding and predicting the unsteadiness of turbulent boundary-layer separation is therefore essential for optimising the performance of aircraft, improving energy efficiency in industrial processes, and mitigating environmental effects in natural fluid systems.

A relatively clear picture can be drawn for the case of geometry-induced turbulent flow separation where fluid particles detach from a solid surface due to a sudden geometry change. Here, along with small-scale turbulent fluctuations and the development of vortical structures inside the separated shear-layer, the dynamics is governed by a low-frequency flapping mode. Eaton & Johnston (1982) showed that the latter resembles an approximately two-dimensional (2-D) vertical motion of the shear-layer. They demonstrated that this leads to an up- and downstream displacement of the reattachment point that terminates the turbulent separation bubble (TSB) induced by a backward-facing step in their study. Further investigations of the flapping motion are concerned with flows past blunt flat plates (Kiya & Sasaki 1983; Cherry, Hillier & Latour 1984; Saathoff & Melbourne 1997), forward-facing steps (Farabee & Casarella 1986; Camussi *et al.* 2008) and a fence-like obstacle (Hudy, Naguib & Humphreys 2003). All of these studies demonstrate the presence of low-frequency unsteadiness consistent with the description by Eaton & Johnston (1982). Furthermore, the associated normalised frequencies $St = f L_b/U_\infty$ are of the same order of magnitude, $\mathcal{O}(St) = 0.1$; here, f denotes the dimensional frequency, L_b is the mean length of the separated flow region and U_∞ is the inflow velocity.

An alternative to the triggering of flow separation through a sudden geometrical change in the bounding surface is the application of an adverse pressure gradient (APG). In contrast, the latter yields a time-dependent location of the separation point, drastically increasing the complexity of flow dynamics, as appreciated by Simpson (1981). The salient low-frequency feature of APG-induced flow separation is a large-scale contraction and expansion of the reverse-flow region. Smith & Kline (1974) conducted flow visualisations in a 2-D diffuser, indicating non-periodic low-frequency changes in the size of the separated flow region. Building on previous studies of the same flow configuration by Fox & Kline (1960), they report that, depending on the flow deflection induced by the diffuser, a partial or complete intermittent wash-out of the recirculating flow can be observed. Similarly, a low-frequency alteration between stalled and unstalled flow on aerofoils was reported by Zaman, McKinzie & Rumsey (1989) and Broeren & Bragg (1998) for angles of attack near the condition of maximum lift. More recently, the unsteadiness of APG-induced TSBs, where both separation and reattachment occurs on a solid flat surface, was addressed by Mohammed-Taifour & Weiss (2016). Based on pressure and velocity field measurements inside the symmetry plane, they reported a low-frequency contraction and expansion of the TSB, named breathing, that takes place at Strouhal numbers of $\mathcal{O}(St) = 0.01$, which is an order of magnitude lower in frequency than the flapping motion found in geometry-induced TSBs.

Along with the flat plate configuration addressed by Mohammed-Taifour & Weiss (2016), the breathing motion of APG-induced TSBs has also been observed for the cases of a 2-D wing (Wang & Ghaemi 2022) and a backward-facing ramp (Steinfurth, Cura & Weiss 2022). Despite the 2-D character of these set-ups, it is well known from surface flow visualisations that there exists a significant secondary flow driven by the presence of sidewalls enclosing the test sections (Mohammed-Taifour, Weiss & Dufresne 2021; Simmons *et al.* 2022). It is therefore reasonable to believe that the low-frequency unsteadiness also features a spanwise component. Indeed, by analysing the results of a direct numerical simulation conducted by Coleman, Rumsey & Spalart (2018),

https://doi.org/10.1017/jfm.2025.10630 Published online by Cambridge University Press

Cura *et al.* (2024) suggested recently that the low-frequency dynamics of APG-induced TSBs are associated with low spanwise wavenumbers. Yet, due to inherent limitations of the methods employed so far, the attention of experimental studies has typically been restricted to events unfolding on the symmetry plane. Notable exceptions are the recent planar velocity field measurements along the test section span presented by Steinfurth *et al.* (2022), Borgmann *et al.* (2024) and Fuchs *et al.* (2025), which all hint at three-dimensional (3-D) flow dynamics.

Contrasting with the experimental studies mentioned earlier, numerical simulations are not *per se* restricted to planar flow field information. However, the computational cost associated with 3-D simulations spanning a number of time steps sufficiently large to resolve the low-frequency spectrum in a wide spanwise domain appears to be unaffordable to date (Na & Moin 1998; Abe 2017; Coleman *et al.* 2018; Wu, Meneveau & Mittal 2020).

In summary, previous studies of TSB low-frequency dynamics were restricted to planar measurements or, in the case of 3-D numerical simulations, could not resolve the low-frequency spectrum. Therefore, a full description of the breathing phenomenon has so far remained elusive, potentially misguiding interpretations of the contraction and expansion unfolding on the TSB symmetry plane. With the current effort, we intend to fill the gap flanked by the 2-D frequency-resolved results obtained in past experiments and the 3-D non-frequency-resolved numerical simulations. Specifically, we conduct volumetric particle tracking velocimetry (PTV) measurements to quantify the time-resolved velocity field for the flow past a smooth backward-facing ramp to reveal a more complete picture of the breathing motion.

2. Experimental approach and data processing

The flow under consideration is characterised in the following before details on the volumetric velocity measurement procedure and data post-processing are provided.

2.1. *Flow configuration*

Experiments were conducted in a low-speed wind tunnel with a $0.6\,\mathrm{m} \times 0.6\,\mathrm{m}$ nozzle exit connected to a 1.2 m long square channel. A splitter plate separates the channel in two parts. The upper side features the smooth backward-facing ramp shown in figure 1(*a*) with dimensions of $l \approx 0.3$ m in length, $H = 0.08$ m in height and $S = 0.6$ m in span. The splitter plate was given a small negative incidence angle (two degrees) to prevent leading-edge separation, resulting in a slightly favourable pressure gradient (FPG) of approximately $\Delta c_p/\Delta x = -0.4\,\mathrm{m}^{-1}$ upstream of the ramp (figure 1*b*). Note that Δc_p is the difference in pressure coefficients between to locations separated by Δx. A local pressure drop near the wall is also expected at the ramp entrance at $x/S = 0$ due to streamline curvature. Further downstream, an APG is observed, ultimately yielding flow separation, visualised with tufts (not shown here) before proceeding with quantitative measurements. The incoming boundary-layer, presented in figures 1(*c*) and 1(*d*), was characterised by displacement and momentum thicknesses of $\delta^* \approx 5.3$ mm and $\vartheta \approx 4.0$ mm, respectively; the resulting shape factor $\delta^*/\vartheta \approx 1.31$ lies at the lower end of the typical range for fully developed turbulent boundary-layers, indicating a low separation tendency. Yet, the scaled profile is well aligned with the logarithmic law of the wall. Based on the momentum thickness and the inflow velocity $U_\infty \approx 6.7\,\mathrm{ms}^{-1}$, the Reynolds number was $Re_\vartheta \approx 1800$.

2.2. *Velocity measurements and data assimilation*

Volumetric velocity field information was obtained by performing 3-D PTV. Helium-filled soap bubbles (HFSBs) with a mean diameter of $d_p \approx 0.3$ mm (Faleiros *et al.* 2019) were

https://doi.org/10.1017/jfm.2025.10630 Published online by Cambridge University Press

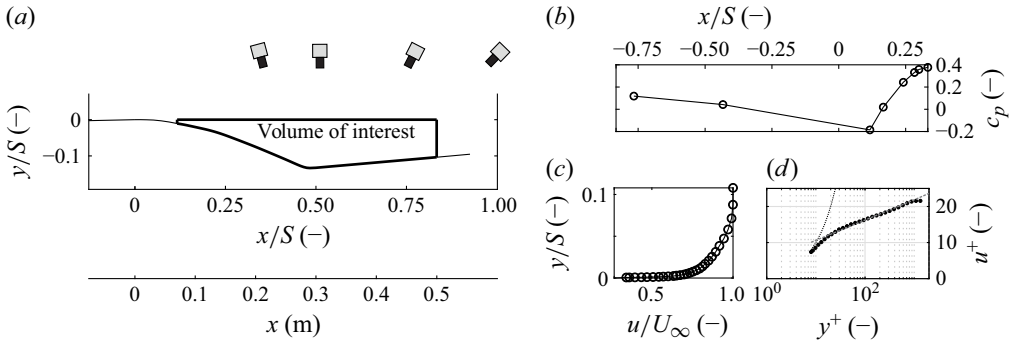


Figure 1. Experimental set-up and inflow conditions: (*a*) schematical side-view of closed test section, camera viewing angles indicated, (*b*) mean wall pressure distribution in the test section centre line, (*c*) and (*d*) mean turbulent boundary-layer profile obtained at $x/S \approx -0.4$; y^+ and u^+ denote the dimensionless wall distance in viscous units and the dimensionless velocity, respectively.

introduced in the settling chamber, with a concentration of approximately $0.25\,\mathrm{cm}^{-3}$ in the test section. The mean particle distance of $\Delta x_p \approx 16$ mm is small compared with the expected length scales associated with the low-frequency unsteadiness. The tracers were illuminated by two arrays of pulsed LEDs (LaVision LED Flashlight 300) placed *vis-à-vis* on both sides of the test section. The illumination was restricted in height to the volume of interest (approximately 100 mm), as shown in figure 1(*a*). The light scattered by HFSB tracers was recorded with four complementary metal-oxide-semiconductor (CMOS) cameras (Photron FASTCAM Mini AX100, 1024 × 1024 pixels at 4 000 f.p.s., pixel size 20 μm × 20 μm) subtending an arc of approximately 60 degrees. Each camera was equipped with a 35 mm photographic lens set with an aperture of $f_\# = 8$. The cameras and LEDs were synchronised with the acquisition computer using a LaVision programmable timing unit (PTU-X). The 3-D particle reconstruction benefited from volumetric self-calibration (Wieneke 2008), and the availability of the Shake-the-Box (STB) algorithm (Schanz, Gesemann & Schröder 2016) involving iterative particle reconstruction and tracking (Wieneke 2013). The component in the x direction for a single time step is highlighted by coloured circles in figures 2(*b*) and 2(*c*).

As is shown in figure 2(*a*), a time-resolved short sequence of eight snapshots was obtained to allow for the application of the STB algorithm with bursts sampled at $f_b = 2$ kHz, returning a velocity field with high accuracy and robustness. However, to cover the relatively wide spectrum of the velocity fluctuations, the frequency of burst repetition was set to $f_s = 60$ Hz. The latter choice allowed velocity measurements over a long observation time (30 s) for a full description of the low-frequency fluctuations in the separated flow. As a result, several events of the breathing motion, expected to occur at a frequency of the order of $f = 1$ Hz (based on pressure measurements), could be captured. The sample rate corresponding to $St > 1$ was chosen such as to also resolve shedding events alongside the breathing.

Physics-informed neural networks (PINNs) were employed to reduce the scattered velocity field vectors onto a Cartesian grid. Equalling the number of detected tracers, approximately 3500 vectors were processed per time step. The approach recently introduced by Steinfurth *et al.* (2024) was followed: fully connected networks consisting of four hidden layers with 256 neurons mapped the spatio–temporal coordinates (x, y, z, t) to the corresponding velocity and pressure values (u, v, w, p). The networks were trained in a supervised fashion, constrained by the PTV data on the one hand and residuals of the 3-D incompressible Navier–Stokes equations on the other. The data and

https://doi.org/10.1017/jfm.2025.10630 Published online by Cambridge University Press

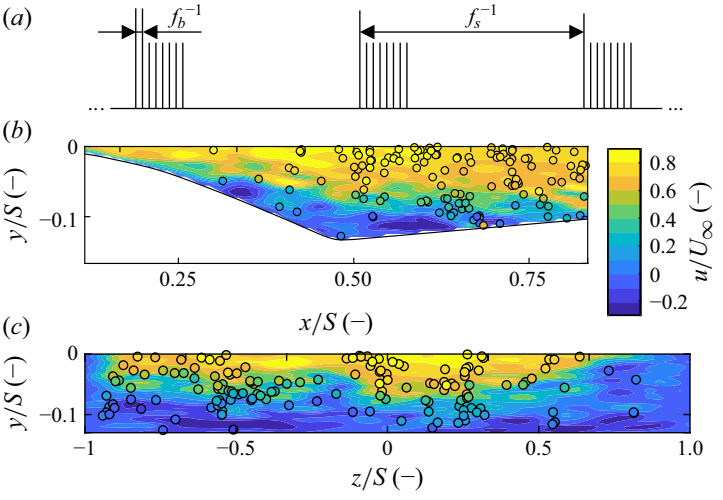


Figure 2. (*a*) Illustration of burst data acquisition, signal defined by burst frequency $f_b = 2000\,\text{Hz}$ and sampling frequency $f_s = 60\,\text{Hz}$, (*b*) instantaneous velocity field in the test section symmetry plane ($z/S = 0$), PTV data with maximum distance of 10 mm from that plane highlighted by circles, assimilated velocity field shown as a contour plot, (*c*) the same as in (*b*) but for a cross-section located at $x/S = 0.5$.

physics-informed losses were evaluated at approximately 3500 PTV measurement points and 3000 randomly sampled collocation points per time step. Furthermore, the no-slip condition was enforced at the solid wall by penalising non-vanishing velocities at 3000 wall points evenly distributed across the solid boundaries. Several PINNs were trained to capture the temporal evolution of the flow field, one for each burst. The target time step corresponded to the fourth sample in the burst sequence. The velocity fields at the preceding and following snapshots were used to determine the time derivatives needed to formulate the physics-informed loss term.

The PINN-based assimilation introduced by Steinfurth *et al.* (2024) was modified in the present study by adopting Fourier feature embeddings mapping the input layer to a higher-dimensional space using a sinusoidal transformation. The transformed input features higher-frequency components compared with the raw input data, which has been shown to address the bias towards learning (only) low-frequency components (Tancik *et al.* 2020). The mean absolute difference between PINN outputs and the PTV measurement data is below $0.01U_\infty$ for the streamwise velocity component. An example of the PINN prediction for a single time step is offered in the shape of heatmaps shown in figure 2, sharing a colour map with the highlighted scattered PTV data.

While the trained models can be inferred at arbitrary locations, we chose to evaluate them only inside the volume of interest (figure 1*a*) with a resolution corresponding to $\Delta x = 5.0\,\text{mm} \approx 0.008S$, $\Delta y = 2.5\,\text{mm} \approx 0.004S$ and $\Delta z = 10.0\,\text{mm} \approx 0.017S$ in the streamwise, vertical and spanwise directions, respectively. The results presented in the following section are based on the analysis of the streamwise velocity component evaluated on structured Cartesian grids with approximately 165 000 points at 1800 time steps (86 points in the x, 32 in the y and 60 in the z direction).

2.3. *Spectral proper orthogonal decomposition*

As opposed to space-only proper orthogonal decomposition (POD), SPOD makes use of temporal Fourier transforms to decompose the flow both in space and in time, providing frequency-dependent modes (Schmidt & Colonius 2020). This allows us to limit our focus

https://doi.org/10.1017/jfm.2025.10630 Published online by Cambridge University Press

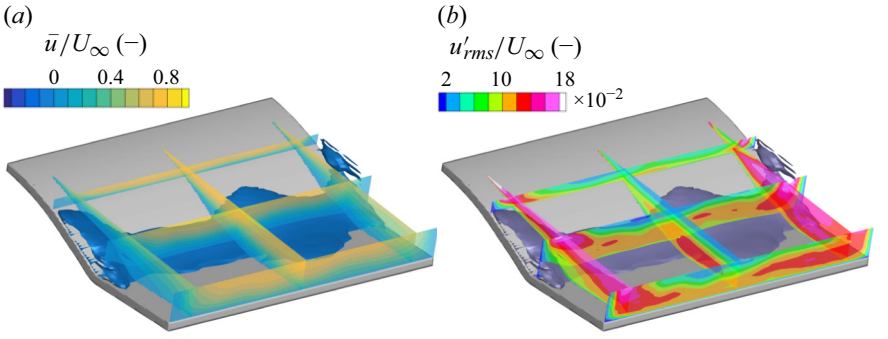


Figure 3. (*a*) Mean streamwise velocity component, the blue isosurface indicates $\bar{u}/U_\infty = 0$, (*b*) normalised root-mean-square of the fluctuating streamwise velocity component $u'_{\mathrm{rms}}/U_\infty$ shown in different slices, $\bar{u}/U_\infty = 0$ now indicated by purple isosurface.

to a specific frequency regime ($St \approx 0.01$) while neglecting spectral content associated with smaller-scale fluctuations. For this analysis, the time series was divided into blocks of 300 snapshots with 50 % overlap. Hamming filters were applied to each block before Fourier transformation. The Fourier coefficients were compiled in cross-spectral density matrices (one for each frequency), and eigendecompositions of these matrices returned the complex-valued SPOD modes ranked by fluctuating energy.

To afford a physical interpretation of the dominant SPOD modes Ψ_u^1 found at low frequencies, the mean flow $\bar{u}(x)$ is superposed by the real part $\mathcal{R}$ of the evolving first mode, defined by

$$u_{\Psi_u^1}(\boldsymbol{x}, t) = \bar{u}(\boldsymbol{x}) + |a^1|\mathcal{R}\big(\Psi_u^1(\boldsymbol{x})\mathrm{e}^{i\omega t}\big), \tag{2.1}$$

where $\omega = 2\pi f$ is the angular frequency of oscillation at the selected frequency $St = 0.02$. Note that the mode is scaled with the related coefficient averaged throughout the time series $|a^1|$, hence the resulting model should be viewed as an idealised harmonic representation of the flow dynamics with a fixed magnitude.

Additionally, dominant SPOD modes were extracted and band-limited to the range $St < 0.05$ following the low-order modelling approach suggested by Nekkanti & Schmidt (2021). An inverse Fourier transform was then applied to recover the time-resolved spatial fluctuations. Finally, the fluctuations were superimposed onto the time-averaged flow field to yield the velocity field evolution over one block duration.

3. Results

Before turning our attention to the 3-D dynamics, it is necessary to characterise the mean field and the breathing signature to relate this study to current state-of-the-art research.

3.1. *Mean field and breathing signature*

Figure 3 shows the time-averaged streamwise velocity component. The mean flow resembles that past a straight backward-facing ramp, addressed by Steinfurth & Weiss (2024): a more distinct inflow velocity deficit is found near the sidewalls compared with the region around the centre line, resulting from the boundary-layers on the sidewalls. Hence, mean reverse flow is observed further upstream in this region. In contrast with the U-shaped mean separation line reported by Steinfurth & Weiss (2024), however, the separation line of the TSB assessed in the present study exhibits a W-shape (i.e. there exists a region close to the centre plane where separation occurs almost as far upstream

https://doi.org/10.1017/jfm.2025.10630 Published online by Cambridge University Press

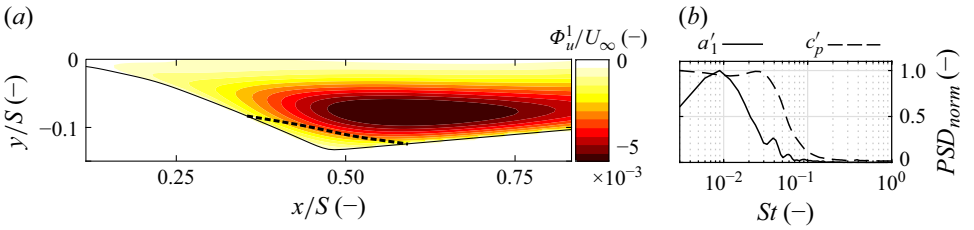


Figure 4. (*a*) Normalised first spatial POD mode Φ_u^1/U_∞ inside the centre plane, dashed line indicates $\bar{u}/U_\infty = 0$, (*b*) normalised power spectral densities PSD_{norm} of fluctuating parts of the first POD coefficient a_1' and wall pressure coefficient c_p' measured at $x/S \approx 0.2$.

as near the sidewalls). This difference in mean flow topology may be caused by minor inflow inhomogeneities. The length of the reverse-flow region inside the centre plane is $L_b \approx S/3$, equalling the aspect ratio found by Steinfurth & Weiss (2024).

The root-mean-square value of streamwise velocity fluctuations u'_{rms} is presented on the right-hand side of figure 3. Strong fluctuations are found throughout the separated shear-layer enclosing the mean TSB, most prominently in the regions close to the sidewalls where values close to 20 % of the inflow velocity are observed. These fluctuations can be expected to originate from two phenomena unfolding in distinct frequency regimes, namely shedding and breathing.

Space-only snapshot POD is applied to streamwise velocity fluctuations inside the centre plane, which has been proven to effectively elucidate the TSB dynamics in previous studies (e.g. Mohammed-Taifour & Weiss 2016). Here, the dominant POD mode, shown in figure 4(*a*), encapsulates more than 70 % of the total kinetic energy and reveals a large region of correlated fluctuations spanning the downstream part of the mean TSB. The physical significance of this observation lies in a large-scale contraction and expansion of the TSB as the modal structure is modulated by the corresponding temporal coefficient a_1. The frequency content of the first POD mode is presented in figure 4(*b*), clearly falling inside the low-frequency regime around $\mathcal{O}(St) = 0.01$. The same is true for the wall pressure obtained upstream of the mean separation line in the region of the highest APG that is known to feature the low-frequency signature of the contraction/expansion motion.

In summary, despite some differences in the mean flow topology, the characteristics pertaining to the low-frequency unsteadiness observed inside the symmetry plane are consistent with findings reported in previous studies that were restricted to planar information.

3.2. *Three-dimensional dynamics*

Next, we turn our attention to the 3-D dynamics revealed by SPOD.

The SPOD spectrum is presented in figure 5(*a*). It shows low-rank behaviour in the range $St < 0.05$ where a large proportion of the fluctuation energy is concentrated in the dominant modes. A minor peak in the leading and sub-leading eigenvalues is observed at $St \approx 0.04$, which is explained by the spectral estimation uncertainty rather than being of physical significance. As a representative of the entire low-frequency regime, we select the dominant SPOD mode at $St \approx 0.02$ ($f = 0.8$ Hz) for further analysis. It contains approximately 50 % of the fluctuation energy at this frequency (figure 5*b*), which is indicative of a dominant physical phenomenon.

The pattern of the dominant SPOD mode (normalised real part) is illustrated in figure 5(*c*). It features four elongated coherent structures with correlated fluctuations. The two smaller ones coincide with the regions of maximum velocity fluctuations near the sidewalls while the larger ones span the flow near the centre plane. Whereas the mode is

https://doi.org/10.1017/jfm.2025.10630 Published online by Cambridge University Press

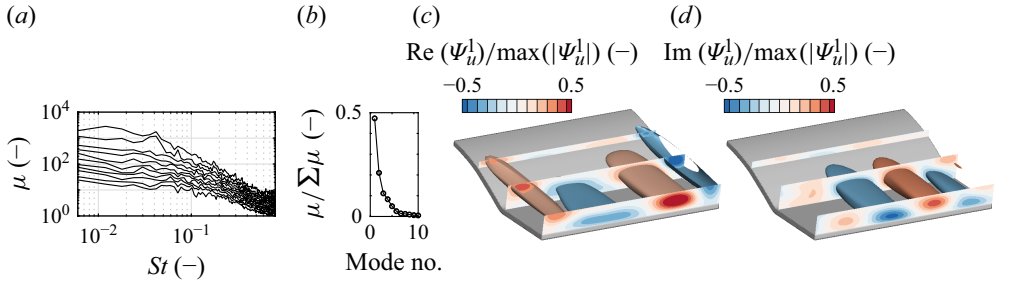


Figure 5. Results of SPOD analysis: (*a*) spectrum of eigenvalues μ, (*b*) fluctuation energy of modes at $St \approx 0.02$, represented by μ relative to sum of all eigenvalues $\sum \mu$, (*c*) and (*d*) isosurfaces highlighting the real and imaginary part of the dominant mode at $St \approx 0.02$, respectively.

relatively homogeneous in the streamwise direction, a cellular pattern of fluctuations is noted along the span. Specifically, a mitigation of the reverse flow near the left sidewall (positive velocity fluctuations) is accompanied by an increase in reverse flow between the centre line and the left sidewall (negative velocity fluctuations), while this pattern is reversed on the other side (i.e. more intense reverse flow close to the right sidewall and reduced TSB between the symmetry plane and the right sidewall).

The imaginary part of the dominant mode is aligned with the real part (figure 5*d*). This in-phase behaviour indicates a standing oscillatory pattern rather than a travelling phenomenon. In other words, the mode is locked in space and oscillates in time. The relative homogeneity in the streamwise direction also suggests that the mode is not of a convective nature. Similar features are found for the dominant modes throughout the low-frequency regime ($St < 0.05$) whereas smaller-scale, convecting structures occur at higher frequencies (not shown here). Both for the real and imaginary part, a spanwise wavelength of $\lambda \approx S/2$ can be estimated visually, corresponding to a wavenumber of two cycles per span. Allowing for a quantitative validation, the complex SPOD mode at $St \approx 0.02$ is decomposed into spanwise wavenumbers k_z by applying a Fast Fourier Transform $\hat{\Psi}_u^1(x, y, k_z) = \mathcal{F}_z[\Psi_u^1(x, y, z)]$ in the cross-section at $x = S/2$ (centre slice in figure 5). The dominant SPOD mode at this location is displayed in figures 6(*a*) and 6(*b*), confirming the high alignment of the real and imaginary parts. In the two-sided wavenumber spectra in figure 6(*c*) for different wall-normal distances, it is apparent that low spanwise wavenumbers carry the majority of the fluctuation energy E. Specifically, a dominant wavenumber of $k_{z,n} = 2$ is found to arise from the low-frequency breathing motion, thereby confirming the visual analysis of 3-D mode structures ($\lambda \approx S/2$). Furthermore, the wavenumber spectra are nearly symmetric about the zero wavenumber (i.e. $E(k_z) \approx E(-k_z)$), indicating that the mode does not contain dominant directionality in the spanwise direction.

Four selected phases of the dynamical process captured by this mode are presented in figure 7(*a–d*). The first time step features an almost symmetric distribution of the cellular reverse-flow regions that occur close to the sidewalls and on both sides of the centre plane, respectively. Next, transitioning from phase $\varphi = \pi/2$ to $\varphi = \pi$, the TSB expands on one side of the backward-facing ramp, namely that which corresponds to the positive (red) streaky structure in figure 5. At the same time, the reverse flow near the respective sidewall is diminished. On the other side of the ramp, the picture is reversed (i.e. the reverse-flow region near the sidewall increases while the TSB close to the centre plane is reduced in size). Finally, at $\varphi = 3\pi/2$ (panel *d*), The maxima/minima associated with the localised reverse-flow region are shifted by $S/3$ in the spanwise direction.

Figure 7(*e*) shows the streamwise distance L_b between the separation and reattachment point observed in the centre plane (black curve) and two further spanwise stations.

https://doi.org/10.1017/jfm.2025.10630 Published online by Cambridge University Press

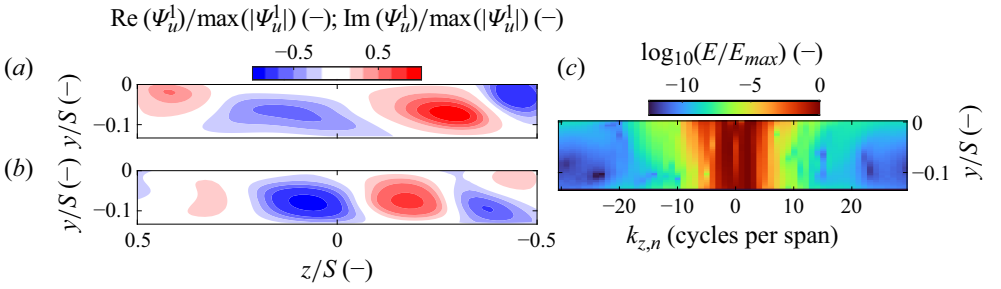


Figure 6. (*a*,*b*) Normalised real and imaginary parts of $St \approx 0.02$ SPOD mode at $x/S = 0.5$, (*c*) wavenumber spectra for different wall-normal distances for these SPOD modes; E and E_{max} denote the raw spectral energy at wavenumber $k_{z,n}$ and the maximum energy at that height, respectively.

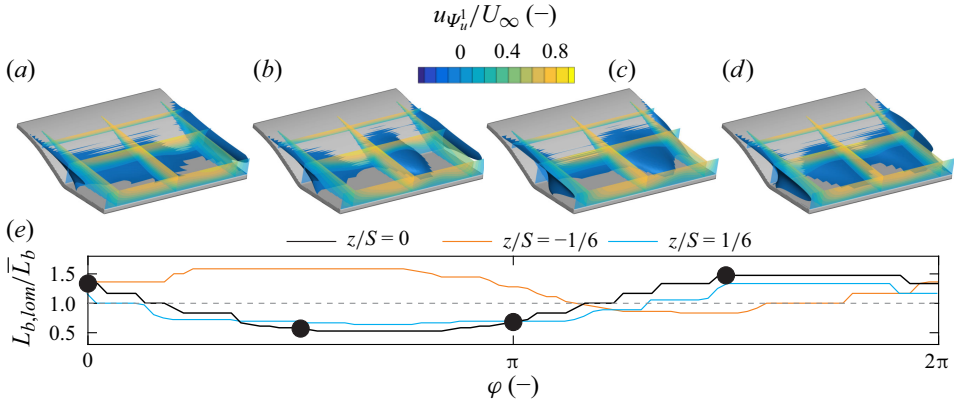


Figure 7. Dynamics represented by leading SPOD mode at $St \approx 0.02$: (*a*) streamwise and crosswise slices indicating the main velocity component along with isosurface defined by $u_{\Psi_u^1}/U_\infty = 0$, shown at phase $\varphi = 0$, (*b*) $\varphi = \pi/2$, (*c*) $\varphi = \pi$, (*d*) $\varphi = 3\pi/2$, (*e*) normalised length of TSB for different spanwise stations throughout one oscillation period, phase angles presented in (*a–d*) highlighted by circles.

The separation/reattachment points are defined by the most upstream/downstream locations where negative streamwise velocity is found. It is immediately apparent that the TSB undergoes significant changes in length during the oscillation (up to $0.5L_b$). This observation is fully consistent with previous studies of the breathing motion limited to planar measurements (e.g. Mohammed-Taifour & Weiss 2016). Here, we demonstrate that this motion is caused by spanwise modulations of the flow field rather than being a 2-D phenomenon.

Similar conclusions can be drawn from the low-order model presented in supplementary movie 1 available at https://doi.org/10.1017/jfm.2025.10630. Here, instead of only one specific frequency, a number of selected frequency bins were utilised to form a low-order representation of the original velocity field dynamics, as explained in § 2.3. The movie clearly indicates that the behaviour observed at $St \approx 0.02$ in figure 7 is in fact representative of a broad low-frequency phenomenon.

4. Concluding remarks

The objective of this study was to elucidate the 3-D low-frequency dynamics of an APG-induced TSB. Although previous works have already reported a large-scale contraction and expansion of the reverse-flow region, they were restricted to planar observations of

https://doi.org/10.1017/jfm.2025.10630 Published online by Cambridge University Press

an intrinsically 3-D dynamical system. The research gap was closed by conducting time-resolved 3-D PTV measurements that quantified the flow in the entire domain of interest and covered the spatio–temporal dynamics of flow separation.

The mean flow, featuring a TSB that spans the entire channel width, is characterised by an inhomogeneous, W-shaped separation line. Specifically, flow reversal is observed the furthest upstream near both sidewalls and close to the centre plane. This observation somewhat differs from the U-shaped topology found in previous experiments (Steinfurth & Weiss 2024) despite the very similar experimental conditions. Nevertheless, the low-frequency signature revealed by space-only POD and wall pressure measurements is consistent with previous experiments.

Spectral proper orthogonal decomposition, applied to fluctuations of the streamwise velocity component, suggests low-rank behaviour at frequencies corresponding to $St < 0.05$, which has been associated with the breathing motion in previous studies. The related dominant modes exhibit inhomogeneities in the spanwise direction at wavelengths of the order of $S/2$. Specifically, one elongated structure is found near each sidewall while two further streaks with larger spanwise extent enclose the mean region of reverse flow near the centre plane. Interestingly, this mirror-inverted pattern is not of a convective nature. Neither does it travel in the spanwise direction but instead represents a standing oscillatory pattern that is locked in space while oscillating in time. The centre node of this standing wave is slightly to the side of the centre plane due to a minor asymmetry ascribed to real-world experimental imperfection. As a consequence, the flow observed in the centre plane experiences significant changes in the extent of the reverse-flow region, which has been observed in previous planar measurements. A similar standing-wave pattern was recently observed by Fuchs *et al.* (2025) for a straight backward-facing ramp. Based on a resolvent analysis, they suggest that this pattern is a consequence of interfering left- and right-travelling modes reflected by the wind tunnel confinement. Furthermore, they associate the formation of the low-frequency streaks with the lift-up mechanism (Brandt 2014).

The cellular standing-wave pattern found in the present study is reminiscent of stall cells occurring on aerofoils and wings (Liu & Nishino 2018). Ma, Gibeau & Ghaemi (2020) recently showed that these localised regions of separated flow undergo low-frequency fluctuations consistent with the breathing phenomenon found in flow configurations where reattachment occurs on a solid surface. Considering that the number of cells strongly depends on the aspect ratio (Weihs & Katz 1983), this parameter and its relation to the resulting low-frequency dynamics may be investigated in future studies.

Supplementary movie. Supplementary movie is available at https://doi.org/10.1017/jfm.2025.10630.

Acknowledgements. The authors gratefully acknowledge funding by the Deutsche Forschungsgemeinschaft (DFG, German Research Foundation) – project number 504349109. We would also like to express our gratitude to C. Cura, L. Fuchs, J. von Saldern and K. Oberleithner for stimulating discussions on TSB dynamics that contributed to the development of this work.

Declaration of interests. The authors report no conflict of interest.

References

Abe, H. 2017 Reynolds-number dependence of wall-pressure fluctuations in a pressure-induced turbulent separation bubble. *J. Fluid. Mech.* **833**, 563–598.

Borgmann, D., Cura, C., Weiss, J. & Little, J. 2024 Three-dimensional nature of low-frequency unsteadiness in a turbulent separation bubble. *AIAA J.* **62** (11), 4349–4363.

Brandt, L. 2014 The lift-up effect: the linear mechanism behind transition and turbulence in shear flows. *Eur. J. Fluid Mech. B/Fluids* **47**, 80–96.

https://doi.org/10.1017/jfm.2025.10630 Published online by Cambridge University Press

BROEREN, A.P. & BRAGG, M.B. 1998 Low-frequency flowfield unsteadiness during airfoil stall and the influence of stall type. In *16th AIAA Applied Aerodynamics Conference*. American Institute of Aeronautics and Astronautics, Inc.

CAMUSSI, R., FELLI, M., PEREIRA, F., ALOISIO, G. & DI MARCO, D. 2008 Statistical properties of wall pressure fluctuations over a forward-facing step. *Phys. Fluids* **20** (7), 075113.

CHERRY, N.J., HILLIER, R. & LATOUR, M.M.M.P. 1984 Unsteady measurements in a separated and reattaching flow. *J. Fluid Mech.* **144**, 13–46.

COLEMAN, G.N., RUMSEY, C.L. & SPALART, P.R. 2018 Numerical study of turbulent separation bubbles with varying pressure gradient and Reynolds number. *J. Fluid Mech.* **847**, 28–70.

CURA, C., HANIFI, A., CAVALIERI, A.V.G. & WEISS, J. 2024 On the low-frequency dynamics of turbulent separation bubbles. *J. Fluid Mech.* **991**, A11.

EATON, J.K. & JOHNSTON, J.P. 1982 Low frequency unsteadyness of a reattaching turbulent shear layer. In *Turbulent Shear Flows 3*, vol. 779. Springer.

FALEIROS, D.E., TUINSTRA, M., SCIACCHITANO, A. & SCARANO, F. 2019 Generation and control of helium-filled soap bubbles for PIV. *Exp. Fluids* **60**, 1–17.

FARABEE, T.M. & CASARELLA, M.J. 1986 Measurements of fluctuating wall pressure for separated/reattached boundary layer flows. *J. Vib. Acoust. Stress Rel. Des.* **108**, 301–307.

FOX, R.W. & KLINE, S.J. 1960 Flow regime data and design methods for curved subsonic diffusers. *J. Basic Eng.* **84**, 303–312.

FUCHS, L.M., STEINFURTH, B., VON SALDERN, J.G.R., WEISS, J. & OBERLEITHNER, K. 2025 A standing-wave model for the low-frequency dynamics of a turbulent separation bubble, arXiv:2505.24723.

HUDY, L.M., NAGUIB, A.M. & HUMPHREYS, W.M., Jr. 2003 Wall-pressure-array measurements beneath a separating/reattaching flow region. *Phys. Fluids* **15**, 706–717.

KIYA, M. & SASAKI, K. 1983 Structure of a turbulent separation bubble. *J. Fluid Mech.* **137**, 83–113.

LIU, D. & NISHINO, T. 2018 Numerical analysis on the oscillation of stall cells over a NACA 0012 aerofoil. *Comput. Fluids* **175**, 246–259.

MA, A., GIBEAU, B. & GHAEMI, S. 2020 Time-resolved topology of turbulent boundary layer separation over the trailing edge of an airfoil. *J. Fluid Mech.* **891**, A1.

MOHAMMED-TAIFOUR, A. & WEISS, J. 2016 Unsteadiness in a large turbulent separation bubble. *J. Fluid Mech.* **799**, 383–412.

MOHAMMED-TAIFOUR, A., WEISS, J. & DUFRESNE, L. 2021 Explicit algebraic Reynolds-stress modeling of pressure-induced separating flows in the presence of sidewalls. *J. Fluids Eng.* **143** (10), 101502.

NA, Y. & MOIN, P. 1998 Direct numerical simulation of a separated turbulent boundary layery. *J. Fluid Mech.* **374**, 379–405.

NEKKANTI, A. & SCHMIDT, O.T. 2021 Frequency–time analysis, low-rank reconstruction and denoising of turbulent flows using SPOD. *J. Fluid Mech.* **926**, A26.

SAATHOFF, P.J. & MELBOURNE, W.H. 1997 Effects of free-stream turbulence on surface pressure fluctuations in a separation bubble. *J. Fluid Mech.* **337**, 1–24.

SCHANZ, D., GESEMANN, S. & SCHRÖDER, A. 2016 Shake-The-Box: Lagrangian particle tracking at high particle image densities. *Exp. Fluids* **57** (70), 1–27.

SCHMIDT, O. & COLONIUS, T. 2020 Guide to spectral proper orthogonal decomposition. *AIAA J.* **58** (3), 1023–1033.

SIMMONS, D.J., THOMAS, F.O., CORKE, T.C. & HUSSAIN, F. 2022 Experimental characterization of smooth body flow separation topography and topology on a two-dimensional geometry of finite span. *J. Fluid Mech.* **944**, A42.

SIMPSON, R.L. 1981 Review - a review of some phenomena in turbulent flow separation. *J. Fluids Engng* **103**, 520–533.

SMITH, C.R., JR & KLINE, S.J. 1974 An experimental investigation of the transitory stall regime in two-dimensional diffusers. *J. Fluids Eng.* **96**, 11–15.

STEINFURTH, B., CURA, C. & WEISS, J. 2022 Three-dimensional effects associated with the low-frequency breathing motion of a turbulent separation bubble. In *20th International Symposium on Application of Laser and Imaging Techniques to Fluid Mechanics*.

STEINFURTH, B., HASSANEIN, A., DOAN, N.A.K. & SCARANO, F. 2024 Physics-informed neural networks for dense reconstruction of vortex rings from particle tracking velocimetry. *Phys. Fluids* **36**, 095110.

STEINFURTH, B. & WEISS, J. 2024 Assimilating experimental data of a mean three-dimensional separated flow using physics-informed neural networks. *Phys. Fluids* **36**, 015131.

TANCIK, M., SRINIVASAN, P.P., MILDENHALL, B., FRIDOVICH-KEIL, S., RAGHAVAN, N., SINGHAL, U., RAMAMOORTHI, R., BARRON, J.T. & NG, R. 2020 Fourier features let networks learn high frequency functions in low dimensional domains. In *34th Conference on Neural Information Processing Systems (NeurIPS 2020)*. Association for Computing Machinery (ACM).

https://doi.org/10.1017/jfm.2025.10630 Published online by Cambridge University Press

WANG, S. & GHAEMI, S. 2022 Unsteady motions in the turbulent separation bubble of a two-dimensional wing. *J. Fluid Mech.* **948**, A3.

WEIHS, D. & KATZ, J. 1983 Cellular patterns in poststall flow over unswept wings. *AIAA J.* **21** (12), 1757–1759.

WIENEKE, B. 2008 Volume self-calibration for 3D particle image velocimetry. *Exp. Fluids* **45**, 549–556.

WIENEKE, B. 2013 Iterative reconstruction of volumetric particle distribution. *Meas. Sci. Technol.* **24**, 024008.

WU, W., MENEVEAU, C. & MITTAL, R. 2020 Spatio-temporal dynamics of turbulent separation bubbles. *J. Fluid Mech.* **883**, A45.

ZAMAN, K.B.M.Q., MCKINZIE, D.J. & RUMSEY, C.L. 1989 A natural low-frequency oscillation of the flow over an airfoil near stalling conditions. *J. Fluid Mech.* **202**, 403–442.

https://doi.org/10.1017/jfm.2025.10630 Published online by Cambridge University Press